Dual phase lag model-based thermal analysis of tissue phantoms using lattice Boltzmann method

Shashank Patidar [a], Sumit Kumar [b], Atul Srivastava [b, *], Suneet Singh [a]

[a] Department of Energy Science and Engineering, Indian Institute of Technology Bombay, Powai, Mumbai 400076, India
[b] Department of Mechanical Engineering, Indian Institute of Technology Bombay, Powai, Mumbai 400076, India

ABSTRACT

The present study is concerned with the development and application of Lattice Boltzmann method-based numerical scheme for investigating the thermal response of laser irradiated biological tissue phantom during laser-based photo-thermal therapy. The Lattice Boltzmann Method (LBM) has been employed for analyzing the transport of short-pulse radiation within the body of the tissue phantom that has been considered as the participating medium. In order to determine the two-dimensional temperature distribution inside the tissue medium, the transient form of radiative transfer equation (RTE) has been coupled with the energy equation modeled based on dual phase lag (DPL) heat conduction framework. The LBM-based solution of the coupled RTE and DPL-based numerical model has been benchmarked against the results available in the literature. Results have been presented in the form of two-dimensional temperature distributions, spatial and temporal profiles of temperatures within the body of the laser-irradiated biological tissue phantoms. Effects of phase lags associated with the heat flux (τ_q) and temperature gradients (τ_T) on the resultant temperature distributions inside the laser irradiated tissue phantom have also been analyzed and discussed. Thereafter, the temperature distribution inside the biological tissue phantom embedded with optical inhomogeneities has been determined using the DPL-based model. Results of the study clearly reveal the successful implementation of LBM-based numerical approach in analyzing the thermal response of laser-irradiated biological tissue phantoms. The inherent properties associated with non-Fourier heat conduction models have also been explicitly brought out in the context of photo-thermal therapy.

© 2015 Elsevier Masson SAS. All rights reserved.

1. Introduction

In the past decade due to the availability of short-pulse lasers, the role of lasers in photo-thermal therapy has grown dramatically, wherein the tissue temperature is raised up to a pre-defined threshold value to destroy the cancerous cells. In order to raise the tissue temperatures, the required amount of heat can be produced by various techniques that include ultrasound, radio-frequency (RF), microwaves, etc. [1]. Of all these available techniques, high power laser-based photo-thermal therapy has gained considerable attention due to the potential of short pulse lasers to confine the temperature rise to specified tissue volume rather than affecting the surrounding normal cells. The fundamental idea behind this technique is the possible conversion of photon energy into thermal energy and the heat thus generated is sufficient to induce cellular damage via processes (effects) such as hyperthermia, coagulation and evaporation [2]. Moreover, as part of the continuing developments in this field, recent advances include the applications of plasmonic gold nanoparticles as the contrast agents, which have demonstrated the potential of enhancing the efficiency of laser-based photo thermal therapy [3–5]. This potential of plasmonic gold nanoparticles is primarily due to their properties of strong absorption and relatively weak scattering that are in contrast with the properties exhibited by normal biological samples (high scattering and weak absorption characteristics). By virtue of these characteristics, the gold nano-particles aid into the localized treatment of the embedded abnormal cells with minimum possible damage to the surrounding healthy cells. The available literature also shows that various shapes, sizes and materials of nanoparticles have been employed by a range of researchers in the context of photo-thermal treatment of tumorous cells [6,7].

* Corresponding author. Tel.: +91 22 25767531; fax: +91 22 25726875.
  E-mail addresses: atulsr@iitb.ac.in, atuldotcom@gmail.com (A. Srivastava).

Nomenclature

		Greek symbols	
		κ_a	absorption coefficient
c	speed of light in medium	σ	scattering coefficient
c_v	specific heat of the tissue	β	extinction coefficient
$f(r,v,t)$	particle distribution function	ε	emissivity
$f^{eq}(r,v,t)$	equilibrium distribution function	$\Delta\Omega$	control angle
G	incident intensity	Φ	scattering phase function
I	intensity	α	thermal diffusivity
I_b	black body intensity	ρ	density
k	thermal conductivity	τ_q	phase lag of heat flux
r	position vector	τ_T	phase lag of temperature gradient
T	temperature	τ	relaxation time in BGK model
t	time		

In view of the fact that the technique of laser-based photo-thermal therapy primarily makes use of the photon energy, it is important to develop a detailed understanding of the phenomenon of light propagation through biological tissues that exhibit both scattering as well as absorption properties and are turbid in nature. By virtue of these properties, the incident laser beam undergoes various processes such as reflection from the interfaces, transmittance, scattering and/or absorption. Of all these events, it is primarily the absorbed component that leads to an increase in the tissue temperature. It has well been established that a rigorous electromagnetic theory based analysis is required for completely understand the various mechanisms associated with light propagation inside the laser-irradiated biological samples, which in itself is a complicated and challenging task. Therefore, various mathematical models of varying degree of complexities have been developed to numerically simulate light transport phenomenon in biological tissues. Of all the available approaches, the radiative transfer theory, originally developed by Chandrasekhar [8], is believed to be the most successful for modeling light transport through biological samples [9–11]. Radiative transfer equation (RTE) is an integro-differential equation. This is complicated because of the presence of an integro-differential term due to in-scattering, which makes RTE highly complex and getting the exact solution becomes a challenging task.

In the recent decade, various numerical methodologies such as Monte Carlo method (MCM), discrete ordinate method (DOM), finite volume method (FVM) etc. have been proposed for generating the complete solution of the RTE. The MCM has been used to model the transient RTE by Schweiger et al. [12] and Guo et al. [13]. However, this method requires a large number of energy bundles for accurate results, hence it is not computationally efficient. Guo and Kumar [14] and Sakami et al. [15] extended the applications of DOM to the 2-D rectangular enclosure. Mishra et al. [16] employed a range of numerical techniques such as DOM, FVM and discrete transfer method (DTM) to solve the transient form of RTE in the context of laser-irradiated one-dimensional participating media. It is pertinent to note here that for applications that involve the interaction of short laser pulses with materials under study e.g. biological samples, one needs to take into account the transient effects and hence it becomes important to consider the complete transient form of RTE [14,15,17].

Brief literature review presented above indicates that the importance of developing fast and accurate numerical schemes for simulating light propagation phenomenon through biological samples has been realized by various researchers in the past. In this context, one of the relatively new numerical schemes, namely the Lattice Boltzmann method (LBM) has attracted the attention of quite a few research groups in the recent past, though it's potential in the field of photo-thermal therapy has not yet been fully explored. In one of the works presented by Asinari et al. [18], the authors employed the LBM to solve the steady-state RTE in a 2-D rectangular enclosure. The numerical study found that LBM provides accurate results, and is also computationally efficient than the FVM-based numerical approach. Mishra and Vernekar [19] extended the work of Asinari et al. [18] to analyze the transport of collimated radiation in one-dimensional planar participating medium. Another study reported by Vernekar and Mishra [20] has been concerned with the transport of short-pulse radiation in one-dimensional planar participating medium. In the recent past, LBM has been widely employed for handling the fluid flow and heat transfer problems [21–23] primarily due to its attractive properties such as relative ease of implementation on computer, mesoscopic nature, ability simulate complex geometries and boundary conditions, and parallelization of computer code [18,24].

In the context of therapeutic applications, one of the primary interests in photo-thermal therapy is to understand the extent of heat diffusion through the body of the laser-irradiated biological samples and the resultant temperature distributions. The correct estimate of thermal profiles becomes important for selective destruction of abnormal cells (malign/benign) present in an otherwise homogeneous medium. While the solution of RTE through any of the above-mentioned numerical schemes provides intensity distribution due to light propagation through the biological samples, the resultant intensity distribution needs to be coupled with a suitable heat conduction model for understanding the thermal response of the medium under study. In this direction, one of the most commonly employed approaches for determining the temperature distribution in laser-irradiated biological samples has been based on Pennes bio-heat transfer equation, as earlier introduced by Pennes [25]. In this approach, the source term is derived from divergence of radiative heat flux that is obtained through the solution of RTE and is coupled with the Penne's bio-heat equation for determining the temperature distribution inside the body of laser-irradiated biological sample. However, one of the major limitations of this approach has been the assumption of infinite speed of thermal wave propagation through the body of the biological sample which is considered to be turbid in nature.

By virtue of the inherent turbidity, the biological samples exhibit absorption as well as scattering properties due to presence of absorbers like water, hemoglobin etc. and scatterers like cell membranes, red-blood cells, etc. The presence of non-homogeneous cell structures acts as additional centers for increasing the turbidity of biological samples and hence a finite phase lag is expected between the heat flux and the resultant

temperature distribution inside the laser-irradiated tissue domain. In this context, non-Fourier heat conduction models have been proposed and developed by quite a few researchers in the recent past for taking into account the finite speed of thermal wave propagation through biological samples. Some of notable studies include the works reported by Cattaneo [26] and Vernotte [27] wherein the authors proposed wave-based hyperbolic heat conduction (HHC) model by introducing relaxation time. Although the paradox of instantaneous response of thermal disturbance can be solved through HHC model, but it also introduces physically un-realizable solutions, as has been demonstrated by a few researchers in the past [28,29]. Along the similar lines, Bright and co-workers have also dwelled upon the possibility of the prediction of unphysical results through HHC models [30,31].

Recently the dual-phase-lag (DPL) heat conduction model pro-posed by Tzou [32] got considerable interest due to its potential importance in areas such as modeling heat conduction in biological materials [33], heat transport in amorphous media [34] etc. This model allows either the temperature gradient to precede the heat flux or the heat flux to precede the temperature gradient, depending upon the relative influence of relaxation times associ-ated with the resultant temperature gradient and/or the heat flux. On the other hand, a select group of authors have also commented on the possible limitations of DPL model. For example, the study reported by Rukolaine [35] for three-dimensional Jeffreys-type equation with a positive localized source of short duration has highlighted such aspects of DPL model. It is important to mention here that though the importance of this generalized non-Fourier heat conduction DPL model in the area of photo-thermal therapy has been realized by various researchers, not much literature exists that focuses on the coupling of DPL model with the transient form of RTE except a very recent work reported by Kumar and Srivastava [9]. The study by Kumar and Srivastava involves the solution of transient form of RTE using DOM while the DPL-based heat con-duction model has been solved using finite volume method (FVM).

With reference to the application of LBM, in one of the recent works, Sun and Zhang [36] solved the conventional Fourier-based heat conduction equation using LBM while the radiative source term in the heat conduction equation was obtained by solving the steady-state RTE using DOM. This study suggests the need of the same grid systems for LBM and DOM, to avoid additional in-terpolations between these two solvers while adding the radiative heat source to the energy equation. However, this study and some of the earlier studies e.g. Refs. [37,38] have primarily been based on two de-coupled approaches, wherein the authors have solved the RTE using the conventional FVM or DOM and the LBM has been employed only for solving the Hyperbolic and Fourier-based heat conduction models. The implementation of two different numerical solvers for separately solving the radiative transfer equation and heat conduction models would require additional interpolations and numerical steps as has been discussed in the study reported by Sun and Zhang [36]. In view of these limitations, development of a uniform numerical methodology for the coupled form of governing equations is desirable. Some of the very few efforts made in this direction include the works of Mishra and co-workers wherein the authors solved the coupled Fourier-based heat conduction equation and RTE using LBM, and found that the LBM−LBM combination is computationally faster than the LBM−FVM [39,40]. However, it is to be noted here that the implementation of LBM-based numerical solver for handling the coupled transient RTE and DPL-based heat conduction model for understanding the thermal response of laser-irradiated biological tissue phantoms has not been reported in the available literature.

With this background, the present work is concerned with the development and application of a uniform LBM-based numerical solver for understanding the thermal response of laser-irradiated biological tissue phantoms using a generalized non-Fourier heat conduction DPL model. The solution of the transient RTE has been coupled with the DPL model to determine the resultant tempera-ture distribution inside the body of single-layered biological tissue phantom. The optical properties of the tissue phantom considered have been kept similar to the biological samples. It is pertinent to note here that the real superficial biological tissues are generally characterized by a layered structure such as epidermis, several layers of dermis, subcutaneous fat layer and more internal tissues, and properties of each of these layers play an important role in influencing the heat transfer processes during the thermal treat-ment of cancerous cells [41,42]. However, in view of the fact that the primary focus of the present work is the development and appli-cation of a uniform LBM-based numerical scheme for the coupled transient RTE and DPL heat conduction model, the numerical studies have been performed on single-layered tissue phantoms for determining the two-dimensional temperature distributions. The numerical code, developed in-house, has first been thoroughly benchmarked against the results available in the published litera-ture. Thereafter, the LBM-based numerical scheme has been implemented for understanding the effects of various parameters like relaxation times associated with heat flux and temperature gradient on the resultant temperature distribution inside the domain of the tissue phantoms. The effects of optical in-homogeneities embedded in an otherwise homogeneous tissue phantoms on the resultant temperature distribution have also been studied and presented. The optical inhomogeneities represent the abnormal cells, generally classified as malignant (absorption in-homogeneity) and/or benign cells (scattering inhomogeneity). The motivation of the study lies in the fact that the localized changes in the absorption and/or scattering coefficient within the spatial extent of the embedded inhomogeneities (malignant/benign) as compared to the surrounding medium influence the light propa-gation through the biological samples, which in turn results in considerable temperature variations inside body of the biological samples.

2. Mathematical formulation

Light propagation through the biological tissue phantom is mathematically modeled by the transient RTE, Eq. (1). Radiation intensity (I) in any direction $\widehat{s}$ identified by a solid angle Ω about the elemental solid angle $\Delta\Omega$ is given by Refs. [11,16]:

$$\frac{1}{c}\frac{\partial I}{\partial t} + \frac{\mathrm{d}I}{\mathrm{d}s} = -\beta I + \frac{\sigma}{4\pi}\int_0^{4\pi} I\phi(\Omega', \Omega)\mathrm{d}\Omega' \tag{1}$$

Eq. (1), that is integro-differential in nature, has first been con-verted into a set of partial differential equation corresponding to a finite number of lattice direction M using D2Q8 model in LBM. The existing numerical methodologies for solving RTE such as DTM, DOM, FVM etc. assume some kind of angular isotropy. However, in LBM, the radiative energy is simulated in terms of particle distri-bution functions (PDFs) and is carried to the neighboring lattices only through some discrete direction. Once the intensity field is known within the tissue phantom, the local temperature distribu-tion due to the single pulse laser irradiation can be obtained by solving Eq. (2).

$$\rho c_{\mathrm{v}}\frac{\partial T(x, y, t)}{\partial t} = -\nabla \cdot q_{\mathrm{r}} \tag{2}$$

where the divergence of the radiative heat flux ($\nabla \cdot q_r$) and incident intensity (G) can be calculated by following expression,

$$\nabla \cdot q_r = \kappa_a(4\pi I_b - G) \tag{3}$$

$$G = \sum_{m=1}^{M} \omega^m I^m \tag{4}$$

Eq. (3) is the divergence of radiative heat flux which represents the net radiative heat loss from the medium. The first term on the right-hand side of Eq. (3) is emission from the medium while the second term is the incident intensity; κ_a is the absorption co-efficients, I_b is the black body intensity and ω is the weight in discrete direction m.

In order to determine the temperature distribution within the body of the biological tissue phantom that is subjected to a train of short laser pulses, the temperature rise obtained from Eq. (2) is added to the temperature value calculated at the previous time step and employed as the initial condition for bio-heat transfer equation (Eq. (5)) in order to determine the temperature distribution at the current time instant [9],

$$\rho c_v \frac{\partial T}{\partial t} = -\frac{(\partial q)}{\partial r} + Q_m + w_b \rho_b c_b (T_b - T) \tag{5}$$

where q is heat flux; ρ and c_v are, respectively, density and specific heat of the tissue; ρ_b and c_b are the density and specific heat of blood, w_b is the blood perfusion rate; T_b and T are the temperature of blood and tissue respectively; Q_m is the source term due to the metabolic heating. The simplest form of DPL with the first order approximations for both q and T is given as follows [43]:

$$q(r,t) + \tau_q \frac{\partial q(r,t)}{\partial t} = -k \left[\frac{\partial T(r,t)}{\partial r} + \tau_T \frac{\partial^3 T}{\partial r^2 \partial t} \right] \tag{6}$$

Here r is the position vector, k is thermal conductivity of the tissue, τ_q is the phase lag time of heat flux, and τ_T is the phase lag time of temperature gradient. Antaki [44] estimated the value of τ_q to be range of 14–16 s while τ_t to be 0.043–0.056 s for the processed meat. Since for normal bodies amount of heat generated due to metabolic activities is very small [45,46], so its contribution towards total heat generation can be neglected compared to the heat generated by incident laser intensity. Furthermore, the numerical simulations reported in the present study have been performed on solid single layer tissue phantoms without the presence of large blood vessels e.g., arteries. The metabolic heat generation and blood perfusion has been neglected. The solution of Eqs. (5) and (6) simultaneously leads to

$$\tau_q \frac{\partial^2 T}{\partial t^2} + \frac{\partial T}{\partial t} = \alpha \frac{\partial^2 T}{\partial r^2} + \alpha \tau_t \frac{\partial^3 T}{\partial r^2 \partial t} \tag{7}$$

The system of equations presented above has been solved under the following assumptions: the boundaries of the medium are non-reflecting and non-refracting, refractive indices of the tissue phantom and the surrounding medium are same. Moreover, the contribution due to the thermal emission from the tissue has been neglected. This assumption can be justified in view of the fact that the blackbody radiation intensity is significantly smaller than the intensity of the short pulse laser employed for irradiating the sample. The assumptions mentioned above are in accordance with the studies earlier reported in the literature [47]. It is also important to mention here that the RTE and the bio-heat transfer equations have been solved at two different times scales; the time scale used for Eqs. (1) and (2) is of the order of picoseconds while time scale

used for Eq. (5) is of the order of milliseconds in order to capture the phenomenon of heat diffusion through the body of the tissue phantom [11].

3. Numerical modeling

A finite two dimensional square enclosure of a biological tissue with dimensions 2 mm × 2 mm and initial temperature of 37 °C is considered in present numerical study. The tissue is irradiated normal incidence on the top wall (as shown in Fig. 1(a)). The top wall of the tissue phantom is subjected to convective boundary conditions with surrounding temperature of $T_\infty = 25$ °C and heat transfer coefficient, $h = 15$ W/(m^2 K) [48], while temperature of the remaining three walls of the phantom is maintained at 37 °C, as shown in Fig. 1(a). The parameters of short pulse laser used for irradiating the tissue are: amplitude of pulse 1.6×10^{-3} J/mm^2/ps, repetition rate 1 kHz and wavelength of 1100 nm. The laser pulses have been modeled as point source with a pulse width of $t_p = 5$ ps. Similar parameters are frequently employed in the medical community for therapeutic applications [49,50]. The values of the absorption (κ_a) and scattering (σ) coefficients are 0.051 mm^{-1} and 6.14 mm^{-1} respectively [11,47]. The thermos-physical properties of the tissue phantom include density (ρ) to be equal to 1000 kg/m^3, thermal conductivity (k) of 0.63 W/m K, while the value of specific heat (c_v) is 4200 J/kg K [11].

3.1. Radiative transfer equation

The RTE has been solved using LBM and the square enclosure has been divided into 51 × 51 lattices. On the basis of a detailed grid independence study, the grid size of 51 × 51 has been chosen for the numerical simulations presented here. In the current LBM-based analysis, the two-dimensional lattice lies in the x–y plane (the solution plane), as schematically shown in Fig. 1(b). In view of the fact that the intensity varies in the 4π spherical space, and assuming isotropy in the polar direction θ ($0 < \theta < \pi$), the angular dependence of intensity is considered only in the azimuthal direction φ ($0 < \varphi < 2\pi$). D2Q8 lattice model (as shown in Fig. 2(a)) has been employed in which the 2π angular space has been discretized into 8 divisions, with all directions being equally-spaced.

Assuming that the medium is non-reflecting, the boundary condition for the collimated and diffused intensity on all the four walls (left, right, bottom and top) of the tissue phantom are given below [11]:

Left wall ($x = 0$, $0 < y < 2$ mm):

$$I_w^m = 0 \text{ for } \mu_m > 0, \quad I_c^m = 0 \text{ for all } \mu_m, \quad \text{and } I_d^m = 0 \text{ for } \mu_m > 0$$

Here I_w^m, is the total intensity (sum of collimated (I_c^m) and diffuse (I_d^m) components) in the discrete direction m and μ and ζ are the direction cosines.

Right wall ($x = 2$ mm, $0 < y < 2$ mm):

$$I_w^m = 0 \text{ for } \mu_m > 0, \quad I_c^m = 0 \text{ for all } \mu_m, \quad \text{and } I_d^m = 0 \text{ for } \mu_m < 0$$

Bottom wall ($y = 0$, $0 < x < 2$ mm):

$$I_w^m = 0 \text{ for } \zeta_m > 0, \quad I_c^m = 0 \text{ for all } \zeta_m, \quad \text{and } I_d^m = 0 \text{ for } \zeta_m > 0$$

Top wall ($y = 2$ mm):

at $y = 2$ mm and $x = 1$ mm : I_c^m
$$= I_0 \big(H(t) - H(t - t_p) \big) \delta(\zeta_m - \zeta_c)$$
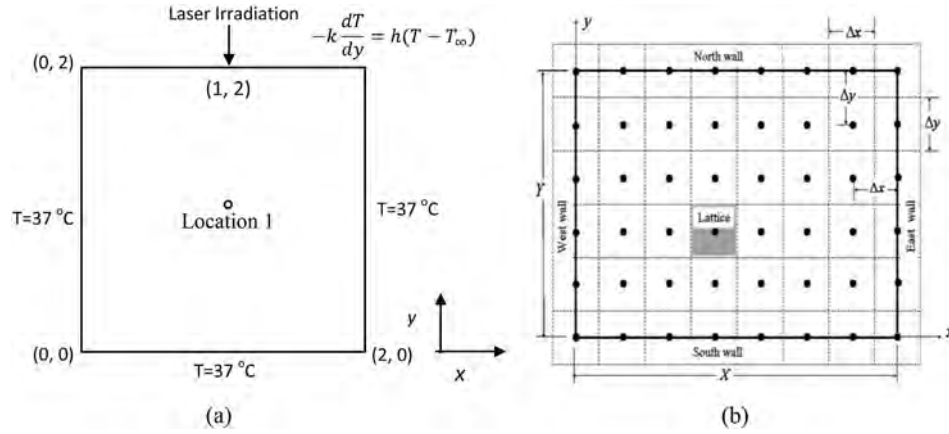
Otherwise at $y = 2$ mm, $I_c^m = 0$

Fig. 1. (a) Schematic diagram of the physical domain under consideration (dimensions in mm); (b) 2-D rectangular geometry and the computational grid [18].
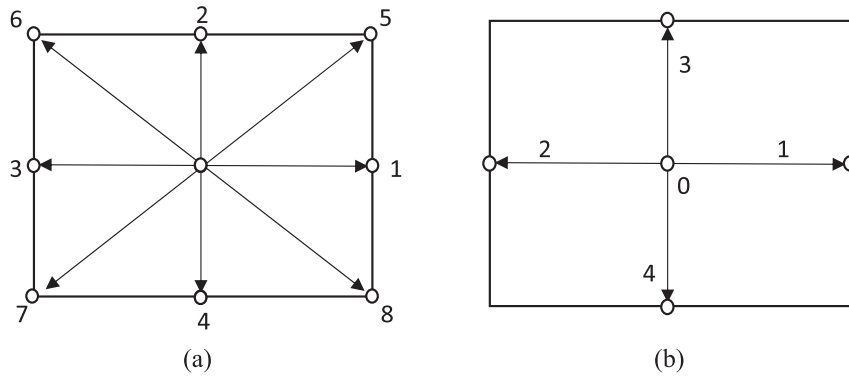

Fig. 2. Schematic of lattices (a) D2Q8 and (b) D2Q5.

For the diffuse component, at $y = 2$ mm and $0 < x < 2$ mm:

$$I_d^m = 0 \text{ for } \zeta_m < 0$$

For solving Eq. (1), the intensity I within the tissue phantom can be expressed as the sum of the collimated intensity I_c and the diffuse intensity I_d.

$$I = I_c + I_d \qquad (8)$$

The variation of the collimated component of the intensity i.e. I_c within the tissue phantom is primarily governed by the Beer's Law [16],

$$\frac{dI_c}{ds} = -\beta I_c \qquad (9)$$

Substituting Eqs. (8) and (9) into Eq. (1) yields

$$\frac{1}{c}\frac{\partial I_d}{\partial t} + \frac{dI_d}{dr} = -\beta I_d + S_t \qquad (10)$$

where S_t is the total source term given by $S_t = S_d + S_c$. S_d and S_c are respectively the source terms due to the diffuse and collimated components on intensity. The phase function ϕ is defined as $\phi(\varOmega',\varOmega) = 1 + a\mu\mu' + a\zeta\zeta'$ and $d\varOmega' = \sin\theta\,d\theta\,d\varphi$.

The collimated residual intensity of the pulse irradiation within the body of the tissue phantom can be expressed as:

$$I_c(s, \varOmega^m, t) = I_0 \exp\left\{-\frac{\beta(L_y - y)}{|\zeta_c|}\right\} \times \left[H\left\{\beta ct - \frac{\beta(L_y - y)}{|\zeta_c|}\right\}\right.$$
$$\left. - H\left\{\left(\beta ct - \frac{\beta(L_y - y)}{|\zeta_c|}\right) - \beta ct_p\right\}\right]$$
$$\times \delta(\mu - \mu_c)\delta(\zeta - \zeta_c)$$

$$\qquad (11)$$

where H is Heaviside function and δ is dirac-delta function, t_p is pulse time and L_y is total length of sample in y direction. Subsequently, Eq. (10) when expressed in terms of the non-dimensional time t^* can be rewritten as

$$\beta\frac{\partial I_d}{\partial t^*} + \frac{dI_d}{dr} + \beta I_d = S_t \qquad (12)$$

where r is the position vector. Using fully implicit backward difference scheme in time, the discretized form of Eq. (12) becomes

$$\beta\frac{I_d - \tilde{I}_d}{\Delta t^*} + \frac{dI_d}{dr} + \beta I_d = S_t \qquad (13)$$

where $\tilde{I}_d$ corresponds to the diffuse component of intensity estimated at the previous time step and Δt^* is the non-dimensional time step.

Rearranging terms in Eq. (13), we get

$$\frac{dI_d}{dr} + \frac{\beta}{B} I_d = S_t + \frac{\beta}{\Delta t^*} \tilde{I}_d \tag{14}$$

where $B = \Delta t^*/(1 + \Delta t^*)$, and the above equation can be rearranged as

$$\frac{dI_d}{dr} = S_t(t^*) + \frac{\beta}{\Delta t^*} \tilde{I}_d - \frac{\beta}{B} I_d \tag{15}$$

Following Refs. [19,20], as part of the implementation of LBM, a pseudo time marching is performed with a M-velocity lattice model in 2-D ($D2QM$) with M being the total number of discrete directions. Along any m^{th} direction, the speed of particle propagation can be shown to be $e_m = \Delta r/\Delta t$.

Applying finite difference discretization scheme to the left hand side of Eq. (15), the transient form of RTE in the mth discrete direction can be expressed as [19,20]

$$\frac{I_d^m(r + e_m \Delta t^*, t + \Delta t^*) - I_d^m(r, t^*)}{\Delta r} = S_t(t^*) + \frac{\beta}{\Delta t^*} \tilde{I}_d - \frac{\beta}{B} I_d \tag{16}$$

where $\Delta r = \sqrt{(\Delta x/\mu)^2 + (\Delta y/\zeta)^2}$, the evolution equation corresponding to Eq. (16) is given as

$$I_d^m(r + e_m \Delta t^*, t + \Delta t^*) = I_d^m(r, t^*) + \Delta t^* e_m \frac{\beta}{B} \left[\frac{B}{\beta} S_t(t^*) \right.$$
$$\left. + \frac{1}{1 + \Delta t^*} \tilde{I}_d - I_d^m(r, t^*) \right] \tag{17}$$

The above equation (Eq. (17)) can be expressed in the standard form of LBM, which is given below

$$I_d^m(r + e_m \Delta t^*, t + \Delta t^*) = I_d^m(r, t^*) + \frac{\Delta t^*}{\tilde{\tau}_m} [\{I_d^m(r, t^*)\}^{eq}$$
$$- I_d^m(r, t^*)] \tag{18}$$

where the $\tilde{\tau}_m$ is the relaxation time for the collision process and $\{I_d^m\}^{eq}$ is the equilibrium particle distribution function. Here, the relaxation time $\tilde{\tau}_m$ is

$$\tilde{\tau}_m = \frac{B}{e_m \beta} \tag{19}$$

and a comparison of Eqs. (17) and (18) gives the equilibrium particle distribution function as

$$\{I_d^m(r, t^*)\}^{eq} = \frac{B}{\beta} S_t(t^*) + \frac{1}{1 + \Delta t^*} \tilde{I}_d \tag{20}$$

The source term S_c and S_d can be calculated as:

$$S_d = \frac{\sigma_s}{4\pi} \int_0^{4\pi} I_d \phi(\Omega', \Omega) d\Omega' \tag{21}$$

$$S_c = \frac{\sigma_s}{4\pi} \int_0^{4\pi} I_c \phi(\Omega', \Omega) d\Omega' \tag{22}$$

3.2. Dual-phase-lag heat conduction equation

The energy equation has also been solved with LBM with physical enclosure divided into same lattice size as used in earlier

section in RTE and D2Q5 model (as shown in Fig. 2(b)) has been used to simulate Eq. (7),

$$\tau_q \frac{\partial^2 T}{\partial t^2} + \frac{\partial T}{\partial t} = \alpha \frac{\partial^2 T}{\partial r^2} + \alpha \tau_t \frac{\partial^3 T}{\partial r^2 \partial t} \tag{23}$$

The kinetic equation for the particle distribution function $f_i(r,t)$, which is the lattice Boltzmann equation (LBE) [51],

$$f_i(r + e_i \Delta t, t + \Delta t) - f_i(r, t) = -\frac{\Delta t}{\tau} \left[f_i(r, t) - f_i^{(0)}(r, t) \right] \tag{24}$$

for $i = 0, 1, ..., b$, where $f_i(r,t)$ denotes the particle distribution functions. Physically, it represents the total number of particles at any given lattice node "r" and at a time instant of t, moving in direction i with velocity e_i along the lattice link $\Delta r_i = e_i \Delta t$ that connects the nearest neighbors. The first term on RHS of Eq. (24) corresponds to the collisions from b directions that drive each distribution (f_i) towards its local equilibrium distribution ($f_i^{(0)}$). Here b is the total no. of directions. Having determined the discrete populations, the macroscopic physical quantity (e.g. temperature field in the present case) can be expressed in terms of the discrete distribution function $f_i(r,t)$ as per the following equation:

$$\tau_q \frac{\partial T(r, t)}{\partial t} = \sum_i f_i(r, t) \tag{25}$$

After using Taylor series expansion, the local temperature at $t + \Delta t$ can be obtained as,

$$T(r, t + \Delta t) = T(r, t) + \Delta t \frac{\partial T(r, t)}{\partial t} + \frac{\Delta t^2}{2} \frac{\partial^2 T(r, t)}{\partial t^2} + O(\Delta t^3) \tag{26}$$

By including heat dissipation term in the extended LBE for DPL equation is proposed as [52],

$$f_i(r + e_i \Delta t, t + \Delta t) - f_i(r, t) = -\frac{\Delta t}{\tau} \left[f_i(r, t) - f_i^{(0)}(r, t) \right]$$
$$- A \Delta t \frac{\partial T(r, t)}{\partial t} \tag{27}$$

In Eq. (27), $f_i(r, t)$ is equilibrium particle distribution function and A is the coefficient to be determined. In the following section, it is demonstrated that this proposed LBE can be macroscopically consistent with the generalized DPL-based bio-heat transfer equation i.e. Eq. (23).

3.2.1. Chapman-Enskog expansion

The existing literature shows that the concept of Chapman-Enskog expansion has well been employed by various researchers for deriving the Navier–Stokes, Euler and other macroscopic equations under the framework of LBM [53,54]. Ho et al. [52] have also reported the derivation of dimensionless form of dual phase lag (DPL) equation for 1-D systems. The following discussion on the Chapman-Enskog expansion (extended for two-dimensional physical domains) has primarily been motivated from the detailed work of Ho et al. [52] reported in the context of 1-D systems.

The Chapman-Enskog expansion is employed to reveal the macroscopic nature of the extended Lattice Boltzmann (LB) equation as it deviates from the equilibrium distribution once disturbed through a small perturbation. Under this scheme, the particle distribution functions (f_i) are subjected to the third order expansion with respect to the expansion parameter δ as,

$$f_i = f_i^{(0)} + f_i^{(1)} + \delta^2 f_i^{(2)} + \delta^3 f_i^{(3)} + O\left(\delta^4\right) \tag{28}$$

where $|\delta| \ll 1$. The nature of the distribution functions is such that their summations should satisfy the following criteria:

$$\sum_i f_i = \sum_i f_i^{(0)} \quad \text{and} \quad \sum_i f_i^{(1)} = \sum_i f_i^{(2)} = \sum_i f_i^{(3)} = 0$$

Changes in the quantities take place both at the temporal as well as space scales and these scales are the large spatial scale $r^{(1)}$, slow time scale $t^{(2)}$ and the fast time scale $t^{(1)}$. One can now express these scalings as

$$\partial_t \approx \delta \partial_{t^{(1)}} + \delta^2 \partial_{t^{(2)}} + \delta^3 \partial_{t^{(3)}} + O\left(\delta^4\right)$$
$$\partial_r \approx \delta \partial_{r^{(1)}} + O\left(\delta^2\right) \tag{29}$$

The heat dissipation term in Eq. (27) is assumed of the scale of $O(\delta^2)$ and can be obtained as,

$$\frac{\partial T}{\partial t} \approx \delta^2 \frac{\partial T}{\partial t^{(2)}} \tag{30}$$

Expanding $f_i(r + e_i \Delta t, t + \Delta t)$ in Eq. (28) around $f_i^{(0)}(r,t)$ up to $O(\Delta t^3)$ and making use of the above mentioned scales, the resulting equations to the order of δ, δ^2 and δ^3 can respectively be given as Eqs. (31)–(33)

$$\partial_{t^{(1)}} f_i^{(0)} + \partial_{r_\alpha^{(1)}} e_{i\alpha} f_i^{(0)} = -\frac{1}{\tau} f_i^{(1)} \tag{31}$$

$$\partial_{t^{(2)}} f_i^{(0)} + \left(-\tau + \frac{\Delta t}{2}\right) \left(\partial_{t^{(1)}} + \partial_{r_\alpha^{(1)}} e_{i\alpha}\right)^2 f_i^{(0)} = -\frac{1}{\tau} f_i^{(2)} - A\frac{\partial T}{\partial t^{(2)}} \tag{32}$$

and,

$$\partial_{t^{(3)}} f_i^{(0)} + (-2\tau + \Delta t)\left(\partial_{t^{(1)}} + \partial_{r_\alpha^{(1)}} e_{i\alpha}\right)\partial_{t^{(2)}} f_i^{(0)} + \left(\tau^2 - \tau\Delta t \right.$$
$$\left. + \frac{\Delta t^2}{6}\right)\left(\partial_{t^{(1)}} + \partial_{r_\alpha^{(1)}} e_{i\alpha}\right)^3 f_i^{(0)}$$
$$= -\frac{1}{\tau} f_i^{(3)} + \tau A\left(\partial_{t^{(1)}} + \partial_{r_\alpha^{(1)}} e_{i\alpha}\right)\frac{\partial T}{\partial t^{(2)}} \tag{33}$$

Eqs. (31)–(33) upon summed up over i in the range of 0 to b result into,

$$\tau_q \partial_{t^{(1)}} \frac{\partial T}{\partial t} + \partial_{r_\alpha^{(1)}} \sum_{i=0}^{b} e_{i\alpha} f_i^{(0)} = 0 \tag{34}$$

$$\tau_q \partial_{t^{(2)}} \frac{\partial T}{\partial t} + \left(\frac{\Delta t}{2} - \tau\right)\left[\tau_q \partial_{t^{(1)}} \partial_{t^{(1)}} \frac{\partial T}{\partial t} + 2\partial_{t^{(1)}} \partial_{r_\alpha^{(1)}} \sum_{i=0}^{b} e_{i\alpha} f_i^{(0)} \right.$$
$$\left. + \partial_{r_\alpha^{(1)}} \partial_{r_\beta^{(1)}} \sum_{i=0}^{b} e_{i\alpha} e_{i\beta} f_i^{(0)}\right]$$
$$= -A(b+1)\partial_{t^{(2)}} T \tag{35}$$

$$\tau_q \partial_{t^{(3)}} \frac{\partial T}{\partial t} + (\Delta t - 2\tau)\left(\tau_q \partial_{t^{(1)}} \partial_{t^{(2)}} \frac{\partial T}{\partial t} + \partial_{r_\alpha^{(1)}} \partial_{t^{(2)}} \sum_{i=0}^{b} e_{i\alpha} f_i^{(0)}\right) + \left(\tau^2 \right.$$
$$\left. - \tau\Delta t + \frac{\Delta t^2}{6}\right)\left(\tau_q \partial_{t^{(1)}} \partial_{t^{(1)}} \frac{\partial T}{\partial t} + 3\partial_{t^{(1)}} \partial_{t^{(1)}} \partial_{r_\alpha^{(1)}} \sum_{i=0}^{b} e_{i\alpha} f_i^{(0)}\right.$$
$$\left. + 3\partial_{t^{(1)}} \partial_{r_\alpha^{(1)}} \partial_{r_\beta^{(1)}} \sum_{i=0}^{b} e_{i\alpha} e_{i\beta} f_i^{(0)} + \partial_{r_\alpha^{(1)}} \partial_{r_\beta^{(1)}} \partial_{r_\gamma^{(1)}} \sum_{i=0}^{b} e_{i\alpha} e_{i\beta} e_{i\gamma} f_i^{(0)}\right)$$
$$= \tau A\left[(b+1)\partial_{t^{(1)}} \partial_{t^{(1)}} T + \partial_{t^{(2)}} \partial_{r_\alpha^{(1)}} \sum_{i=0}^{b} e_{i\alpha} f_i^{(0)}\right] \tag{36}$$

On solving (Eq. (34)) $\times \delta$ + (Eq. (35)) $\times \delta^2$ + (Eq. (36)) $\times \delta^3$ and applying the following constraints,

$$\sum_{i=0}^{b} e_{i\alpha} f_i^{(0)} = 0$$
$$\sum_{i=0}^{b} e_{i\alpha} e_{i\beta} f_i^{(0)} = \lambda T + \tau_T \gamma \frac{\partial T}{\partial t} \tag{37}$$
$$\sum_{i=0}^{b} e_{i\alpha} e_{i\beta} e_{i\gamma} f_i^{(0)} = 0$$

leads to,

$$\tau_q \frac{\partial^2 T(r,t)}{\partial^2 t} + A(b+1)\frac{\partial T}{\partial t} = \left(\tau - \frac{\Delta t}{2}\right)\lambda \frac{\partial^2 T(r,t)}{\partial r^2}$$
$$+ \left(\tau - \frac{\Delta t}{2}\right)\tau_T \gamma \frac{\partial^3 T(r,t)}{\partial r^2 \partial t}$$
$$+ \tau A\delta^3 (b+1)\partial_{t^{(1)}} \partial_{t^{(1)}} T - 3\delta^3\left(\tau^2 \right.$$
$$\left. - \tau\Delta t + \frac{\Delta t^2}{6}\right)\partial_{t^{(1)}} \partial_{r_\alpha^{(1)}} \partial_{r_\beta^{(1)}}\left(\lambda T \right.$$
$$\left. + \tau_T \gamma \frac{\partial T}{\partial t}\right) + O\left(\Delta t^3\right) + O\left(\delta^4\right) \tag{38}$$

As Δt and δ are relatively very small quantities (approaching zero), it is to be seen that Eq. (38) is consistent with Eq. (23) when one chooses A, λ and γ in such a way that $A = 1/(b+1)$ and $\gamma = \lambda = \alpha/(\tau - (\Delta t/2))$. The truncation error obtained after the application of Chapman-Enskog expansion for Eq. (27) can be determined as,

$$R_E = \tau A\delta^3 (b+1)\partial_{t^{(1)}} \partial_{t^{(1)}} T - 3\delta^3\left(\tau^2 - \tau\Delta t + \frac{\Delta t^2}{6}\right)\partial_{t^{(1)}} \partial_{r_\alpha^{(1)}} \partial_{r_\beta^{(1)}}\left(\lambda T \right.$$
$$\left. + \tau_T \gamma \frac{\partial T}{\partial t}\right) + O\left(\Delta t^3\right) + O\left(\delta^4\right) \tag{39}$$

Mathematically, R_E represents the error between the proposed Lattice Boltzmann Equation (27) for solving Eq. (23) and original solution of Equation (23) [52].

The D2Q5 lattice, as schematically shown in Fig. 2(a), with $b = 4$, $e_0 = 0, e_1 = e\hat{i}, e_2 = -e\hat{i}, e_3 = e\hat{j}, e_4 = -e\hat{j}$ has been used for the two dimensional study [52]. The equilibrium particle distribution function, $f_i^{(0)}$ can be determined by $\sum f_i^{(0)} = \tau_q(\partial T/\partial t)$ and the constraints given by Eq. (37), which finally yield,

$$f_0^{(0)} = \tau_q \frac{\partial T}{\partial t} - 2\frac{\lambda}{e^2}T - 2\frac{\tau_T \gamma}{e^2}\frac{\partial T}{\partial t}$$

$$f_1^{(0)} = f_2^{(0)} = f_3^{(0)} = f_4^{(0)} = \frac{1}{2}\frac{\lambda}{e^2}T + \frac{1}{2}\frac{\tau_T \gamma}{e^2}\frac{\partial T}{\partial t} \qquad (40)$$

4. Results and discussion

Primary findings of the LBM-based numerical simulations performed for determining the temperature field distribution within the body of the laser-irradiated tissue phantoms have been presented in this section. First, the LBM-based numerical code developed in the present study has been verified against the results reported in the literature. This verification study has been performed under identical operating parameters. Thereafter, two dimensional temperature distributions, temperature profiles and heat flux profiles inside the laser-irradiated biological tissue phantoms have been presented and discussed. The effects of phase lags associated with heat flux and temperature gradients on the thermal profiles have been presented. Thereafter, the influence of an optical inhomogeneity embedded in an otherwise homogenous medium on the resultant temperature distributions and temperature profiles have been assessed and also compared with the case of the uniformly homogeneous sample. Here the optical inhomogeneity represents the malignant (absorbing inhomogeneity) and benign (scattering inhomogeneity) cells. The inhomogeneities embedded into tissue phantoms have been simulated as the 2-D localized region in which the optical properties (absorption/scattering coefficients) are significantly different from the rest of background homogeneous properties.

4.1. Code verification

Benchmark studies on code verification have been performed on two dimensional enclosures, for radiative transfer part as well as heat conduction part. Fig. 3 shows the benchmark results for the solution of RTE using LBM in the context of two-dimensional planar medium that is subjected to single pulse laser irradiation. Spatial variation of diffused intensity component with respect to the depth of the tissues phantom recorded at $x = 0.98$ mm has been shown in Fig. 3(a). It is to be seen from the figure that the

maxima of the diffuse component is observed at a spatial location that is situated at some distance below the top surface ($y = 2$ mm) of the laser-irradiated tissue phantom. The observation of the maxima of the diffuse component of the intensity can be explained on the basis of the fact that the tissue phantom being turbid in nature exhibits the scattering properties, which in turn affect the propagation of the diffuse component of light intensity. Once the laser power is switched off ($t > 5$ ps), the diffuse component of intensity decreases due to less incoming of photons from top surface, as it can be observed at $t = 14$ ps from Fig. 3(a). The temporal profile of temperature rise (δT) recorded at the point of laser irradiation as obtained through LBM-based solution has been compared with those reported by Kumar and Srivastava [11] and is shown in Fig. 3(b) for the same operating conditions. It is to be seen from the figure that during the first 5 ps, the rate at which the temperature rises is quite rapid as the pulse width of the laser is 5 ps and therefore the laser power is available for this complete duration of $0 < t < 5$ ps. After the laser power is switched off ($t > 5$ ps), the rise in temperature becomes fairly constant due to the fact that net radiative heat flux becomes zero and radiative equilibrium is achieved in the tissue phantom. The above discussion based on the verification results presented in Fig. 3 shows that the developed LBM-based numerical model successfully predicts the process of light propagation through a planar medium that is turbid in nature. Moreover, the results of the present study are reasonably in good agreement with those reported in Ref. [11].

The benchmark study of LBM-based approach for solving the heat conduction model has been carried out by comparing the spatial distribution of temperature field estimated through the solution of hyperbolic heat conduction model with those reported by Yang [55] under the same operating conditions. With reference to the two-dimensional physical domain considered in the work of Yang [55], the following boundary conditions have been employed for the present benchmark study: Top and bottom boundaries: Insulated; Right boundary: maintained at zero non-dimensional temperature; the left boundary is divided into three parts. The boundary condition of constant dimensionless temperature has been imposed at the central 1/3rd portion of the left boundary while the remaining two portions are kept insulated. The dual phase lag model developed in the present work has been converted into hyperbolic heat conduction model by setting the relaxation

(a) (b)
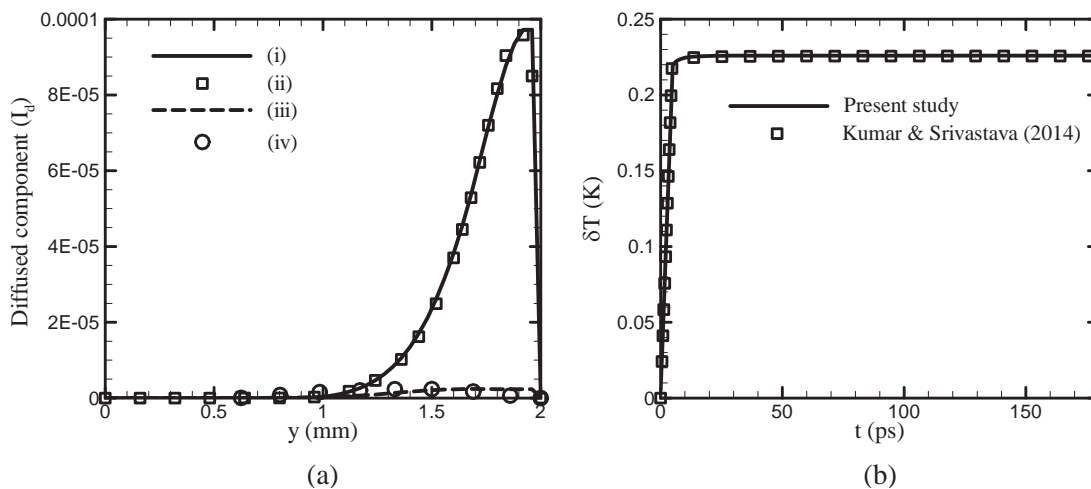
Fig. 3. Comparison of (a) spatial variation of diffuse component of light along a section passing through $x = 0.98$ mm, (i) Present study ($t = 5$ ps), (ii) Kumar & Srivastava (2014) ($t = 5$ ps), (iii) Present study ($t = 14$ ps), (iv) Kumar & Srivastava (2014) ($t = 14$ ps); (b) temporal profile of temperature rise in tissue subjected to single pulse laser irradiation at point of irradiation between present work and Kumar and Srivastava [11].

time associated with the temperature gradient (τ_T) i.e. equal to zero.

Fig. 4(a) shows the temperature distribution as a function of the horizontal direction at a dimensionless height of 0.45 at two different time (ζ) instants. It is to be seen from the figure that the temperature profiles during the initial time instants ($\zeta \leq 1.5$ s) are oscillatory in nature with a certain degree of waviness that one associates with the inherent nature of hyperbolic heat conduction model. The waviness in the temperature variations is much more pronounced in the profiles corresponding to relatively lower values of non-dimensional time instants, e.g. $\zeta = 0.3$ and 0.5. However, as the time progresses, these oscillations tend to die out and nearly steady state conditions are achieved, as signified by an almost linear temperature profile seen at $\zeta = 5$.

The above-presented discussion on the studies performed for code verification pertained to the conversion of the generalized DPL-based heat conduction model into the hyperbolic heat conduction model (HHC) for two-dimensional systems. In order to assess the ability of the numerical scheme developed in the present work for the complete DPL model, select verification studies in the context of one-dimensional physical domain have also been performed with the literature available. For this study, the two-dimensional physical domain shown in Fig. 1(a) has been converted into 1-D system by stretching one of its dimension to a fairly large value and the necessary numerical simulations have then been performed for this geometry using the developed numerical code for the generalized DPL-based heat conduction model. Fig. 4(b) shows the comparison of temperature profiles thus obtained for the 1-D system with those reported by Tzou [32] for different values of non-dimensional relaxation times associated with temperature gradient ($Z_T = 0$, 0.001, 0.05 and 0.5). For these simulations, the value of relaxation time corresponding to heat flux i.e. Z_q has been fixed at 0.05. The effect of increasing value of Z_T on the resultant non-dimensional temperature profiles is clearly to be seen from the figure. At relatively lower values of Z_T (=0 and 0.001), the predicted temperature profiles show the dominance of sharp wave fronts. However, as the relaxation time is increased ($Z_T = 0.05$ and 0.5), the dominant effects of thermal diffusion are clearly to be seen as the temperature profiles tend to get smoothen out and one does not observe sharp wave fronts that were observed for the lower values of Z_T. In addition, a close match between the profiles

obtained in the present work with those reported by Tzou [32] is also to be seen from the figure. Comparison of the temperature profiles at various time instants as obtained through the present LBM-based numerical analysis with those reported in the literature [32,55] reveals a reasonably good match, which verified the code developed in the present work. Moreover, the above discussions pertaining to the benchmark studies on RTE and heat conduction model show that the LBM-based numerical scheme successfully captures the physical phenomenon associated with the thermal response of laser-irradiated tissue phantom.

4.2. Temperature distribution inside a homogeneous tissue phantom

The LBM-based numerical model, thus benchmarked, has now been implemented for determining the two-dimensional temperature distribution within the body of the laser-irradiated homogenous biological tissue phantom. The physical domain under consideration has earlier been schematically shown in Fig. 1(a). The source term in the energy equation has been calculated from the solution of the transient RTE obtained in the form of light intensity distribution within the body of tissue phantom (Eq. (3)). It is pertinent to note here that in photo-thermal therapy, one needs to achieve the localized heating of the abnormal cells (i.e. the target region) without crossing the threshold temperature of the surrounding normal cells. Therefore, it becomes imperative to assess the range of the spatial spread of the thermal energy around the target cell due to the incident laser beam and the resultant temperature distribution in the region of interest.

The two-dimensional distribution of temperature within the body of the tissue phantom at various time instants as predicted using the DPL-based model has been shown in Fig. 5. The relaxation times associated with the heat flux (τ_q) and temperature gradients (τ_T) are respectively equal to 15 s and 0.05 s. It is to be observed that for the initial times instants of laser-irradiation ($t \approx 0.1$ s), the high temperature zone (due to the deposition of the thermal energy), is predominantly localized within the small region surrounding the point of laser irradiation. As the time progresses, the thermal diffusion front propagates through the body of the tissue phantom to the opposite boundary. The two-dimensional temperature distributions, as predicted through the DPL model, are in sharp
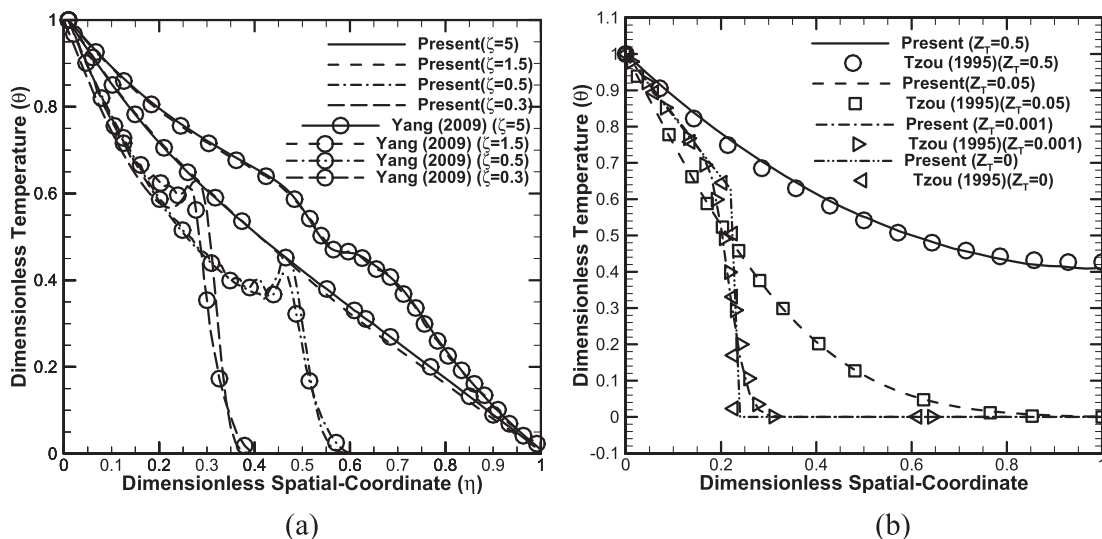

Fig. 4. (a) Spatial distribution of temperature at a dimensionless height of 0.45 at two different time instants; (b) Comparison of non-dimensional temperature profiles obtained for different values of relaxation time associated with temperature gradients (Z_T) as predicted in the present work with those reported by Tzou [32] for a 1-D system.
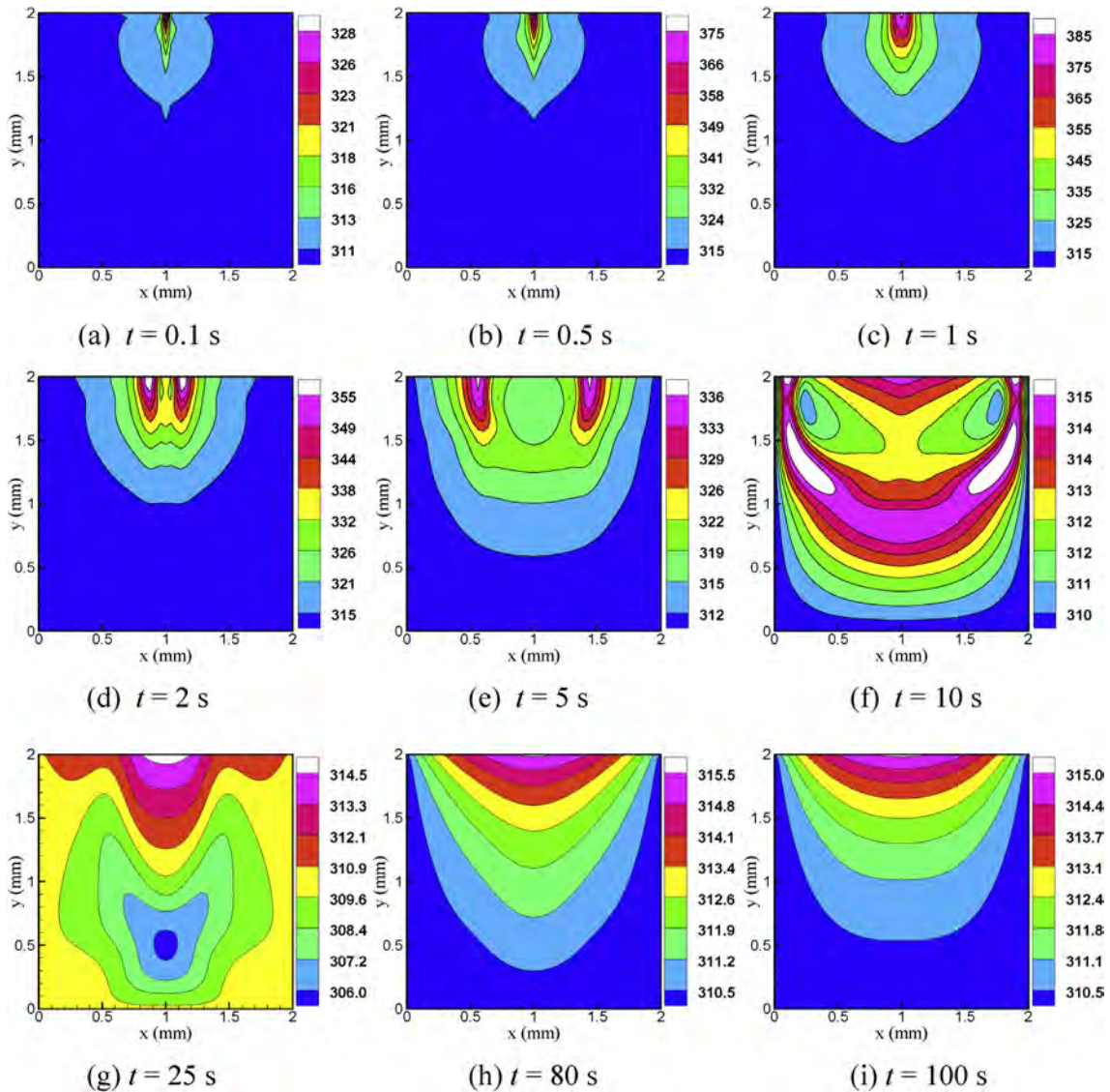
Fig. 5. Two-dimensional temperature distributions within the body of tissue phantom as a function of time due to the train of pulses with a repetition rate of 1 kHz.

contrast with those obtained on the basis of Fourier heat conduction model, as reported in the literature [11]. While a nearly uniform diffusion of thermal energy is predicted via Fourier model, the DPL model-based temperature contours reveal that the temperature field undergoes localized heating and cooling process, as can be seen from the periodic changes in the color shades of temperature contours at any given spatial location within the body of the tissue phantom shown in Fig. 5. The observed heating and cooling behavior and the associated periodic fluctuations in temperature profiles at any given spatial location are to be attributed to the wave nature of the thermal front propagating through the turbid biological phantom, as predicted using the DPL-based heat conduction model. Similar observations have also been reported in the work presented by Shen and Zhang [56] wherein the authors employed a purely numerical explicit total-variation-diminishing (TVD) scheme.

With reference to the temperature contours shown in Fig. 5, it is to be seen that the highest temperature at any given spatial location within the tissue phantom is realized at $t = 1.0$ s. This is understandable since $t = 1.0$ s also happens to be the total time for which the tissue phantom is subjected to laser irradiation.

Once the laser power is turned-off ($t > 1.0$ s), the temperature values start getting reduced. It is worth noting here that the minimum temperature attained inside the tissue sample at $t \cong 25$ s is equal to ≈ 306 K, as shown in Fig. 5(g). This observation is primarily to be attributed to the inherent wave nature of the thermal propagation front that is associated with the non-Fourier heat conductions models, e.g. DPL model in the present work. It can also be seen that slowly the temperature profiles converge towards uniform temperature distribution throughout the body of the tissue phantom. Along the expected lines, the maximum temperature rise ($\Delta T \approx 70$ K) occurs at the point of laser irradiation at $t = 1$ s.

Fig. 6(a) shows the temperature variation as a function of spatial dimension in the x-direction for varying depths of the tissue phantom. It is to be seen from the figure that the temperature values at any particular depth achieve maxima at $x = 1$ mm. This is expected since the direction of laser beam employed for irradiating the tissue phantom is along the vertical section defined at $x = 1$ mm. Thus, the maximum temperature is achieved at the point of laser irradiation i.e. $x = 1$ mm, $y = 2$ mm and is equal to $T_{max} \approx 388$ K.
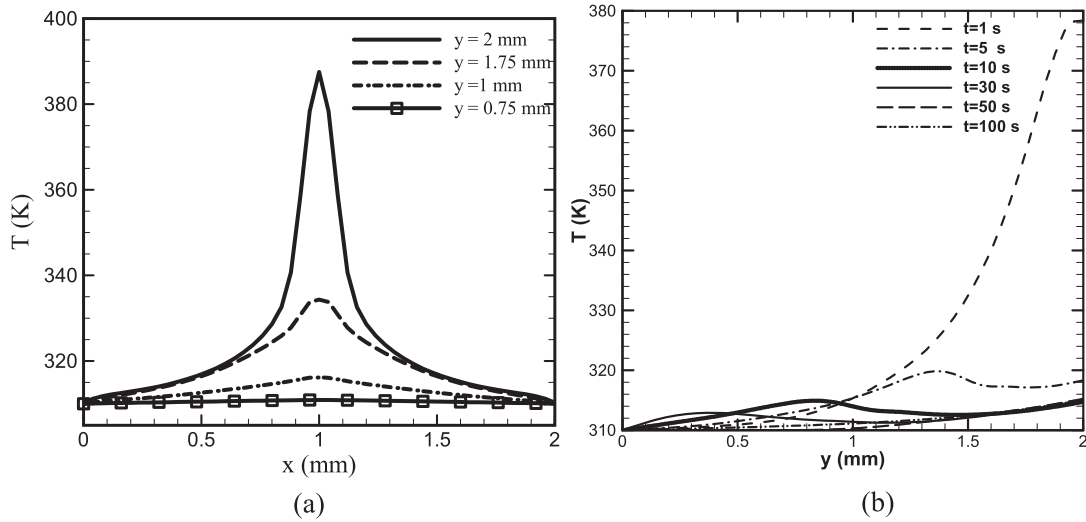
Fig. 6. (a) Spatial variation of temperature at $t = 1$ s at various depths; (b) Variation of temperature with respect to the depth of the tissue phantom at different time instants.

In order to check the ability of the developed numerical scheme for predicting the wave nature of the thermal front propagation, the variation of temperature at a given horizontal section of $x = 1$ mm with respect to the depth of the tissue phantom (y) have been plotted at different time instants and shown in Fig. 6(b). The maximum temperature is realized at the point of laser irradiation i.e. $y = 2$ mm and $t = 1$ s. For higher time instants (e.g. $t = 5, 10, …$,100 s), as the laser power has been switched-off, the temperature values show a significant reduction and the wave nature of the thermal front propagating through the depth of the tissue phantom is to be clearly seen.

The effects of two important parameters in the form of relaxation times associated with the temperature gradient (τ_T) and heat flux (τ_q) on the resultant temperature distribution as well as on the heat flux within the body of the tissue phantom are discussed now. Fig. 7(a) and (b) respectively show the temporal variations of temperature and heat flux (q) at the center of the tissue phantom domain (Location 1 as shown in Fig. 1(a)) for $\tau_q = 10$ s for different values of τ_T while the relaxation time associated with the heat flux i.e. τ_q has been fixed at 10 s. It is evident from Fig. 7(a) that as τ_T increases, the inherent oscillations associated with the temperature

profiles get suppressed and the wave front tends to become more smoother. The phase lag associated with the temperature gradient τ_T leads to significant attenuation of the sharp wave fronts through the diffusion process. A reduction in the maximum magnitude of temperature at time instant ($t \approx 6$ s) is to be seen from Fig. 7(a) with increasing value of τ_T.

It can be seen that the maximum temperature attained for $\tau_T = 0.1$ s and $\tau_T = 0.0001$ s is nearly equal to 316.5 K at $t = 7$ s whereas for $\tau_T = 1$ s, it is 316 K (as shown in the inset of Fig. 7(a)). It is to be noted here that the present discussion pertains to the case wherein the relaxation time associated with the heat flux i.e. τ_q is significantly larger than that associated with temperature gradient (τ_T). Hence it is expected that in comparison with the heat flux, temperature gradients get established within the body of the tissue phantom at a much faster rate. This observation can clearly be made through the time variation of heat flux, as presented in Fig. 7(b) for different values of τ_T. In Fig. 7(b), it can be observed that larger shift in the peak of heat flux on the time scales (x-axis) corresponds to $\tau_T = 1$ s, which implies that τ_T is significantly affecting the heat flux. Due to the higher value of τ_T larger delay in the heat diffusion process
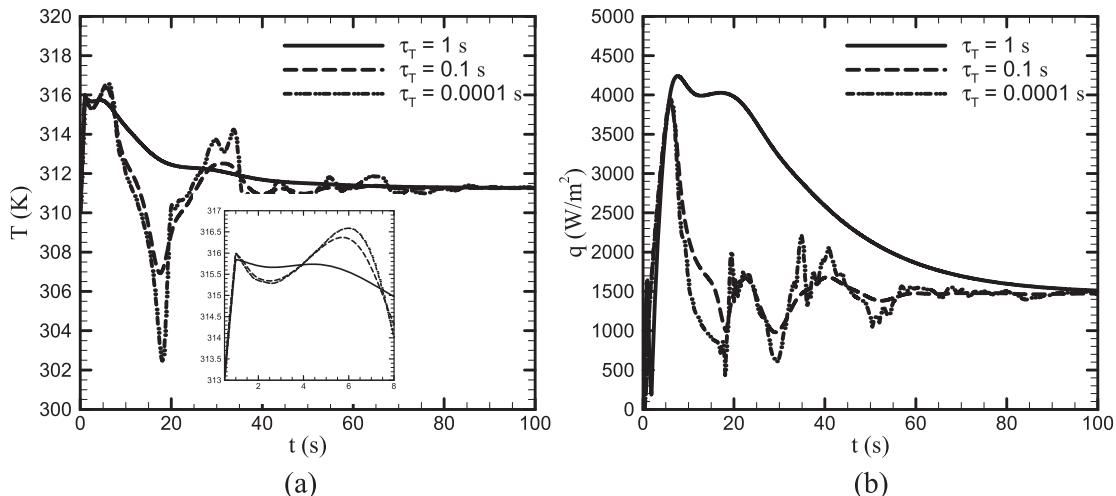

Fig. 7. Temporal distribution of (a) temperature, (b) heat flux at center (Location 1) for $\tau_q = 10$ s.

occurs, thereby causing a time delay in achieving the maximum value of heat flux.

The effects of changes in the relaxation times associated with the heat flux i.e. τ_q on the temporal profiles of temperature distribution and heat flux is depicted in Fig. 8(a) and (b) respectively. The values of τ_q have been varied in the range of 1 s to 20 s while the relaxation time concerned with temperature gradient has been fixed at $\tau_T = 0.1$ s. It is to be seen from Fig. 8(a) that as τ_q increases, the maximum value of temperature and the time required to achieve this maxima in temperature values also increase. The observed trend can be attributed to the fact that as the relaxation time associated with the heat flux (τ_q) increases, the process of diffusion of heat into the rest of the surrounding medium takes relatively longer time, thereby leading to a localized increase in the temperature values at the point of consideration within the body of the tissue phantom. Increase in the time required for heat diffusion also explains the time delay observed in achieving the maximum values of temperatures in Fig. 8(a) with increasing values of τ_q.

Similar observations can also be made from Fig. 8(b) wherein one can see that the maximum value of heat flux is relatively lower for larger values of τ_q. With reference to temperature profiles shown in Fig. 8(a), an enclosed waviness (larger magnitude of oscillations) is to be observed for higher values of τ_q. On the other hand, the temperature variations corresponding to smaller values of τ_q (for instance $\tau_q = 1$ s) show relatively smoother profiles with respect to time.

It has well been established and reported by various researchers that in the context of biological samples, the relaxation time corresponding to the heat flux (τ_q) is comparatively higher than τ_T [9,44,47,57]. This characteristic of the biological samples forms the basis of the choice of the relative values of relaxation times considered in the present study as the primary focus of the present work is to understand the thermal response of laser-irradiated biological tissue phantoms. However, for general interest, it is to be mentioned here that an interesting aspect of the generalized DPL-based heat conduction model is its possible conversion into Fourier-based heat conduction model under the conditions of both the relaxation times (τ_q and τ_T) being equal to each other and have been presented in Fig. 9. Figure shows the temperature profiles as the function of time for two cases: 1) different values of τ_q and τ_T and, 2) both the relaxation times being equal to each other.

With respect to Fig. 9, strong oscillations are to be seen in the temperature profile corresponding to the case wherein the values
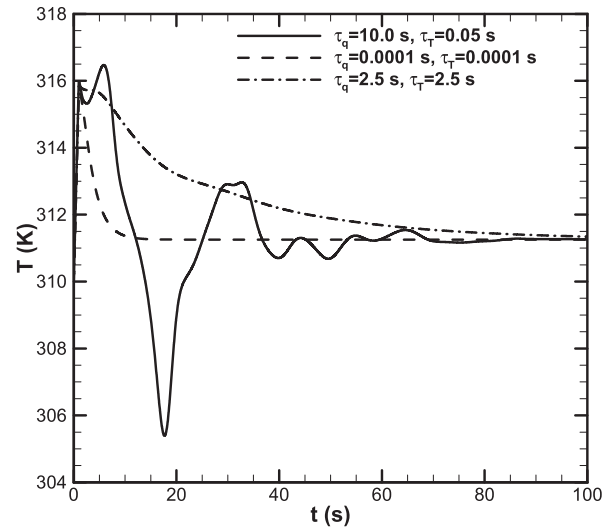

Fig. 9. Temporal variation of temperature for different relative values of relaxation times associated with the heat flux (τ_q) and temperature gradients (τ_T).

of τ_q and τ_T are finite and significantly different from each other. However, the profiles obtained through DPL-based heat conduction model are much smoother and approach towards those similar to Fourier model for the second case wherein the associated relaxation times are equal to each other. It is to be seen that the conditions of thermal equilibrium are achieved much faster for significantly small and equal values of τ_q and τ_T as compared to their relatively higher values. Such features of the dual phase lag heat conduction models can also be seen in one of the recent works of the authors [9].

4.3. Thermal response of biological phantom with embedded inhomogeneity

The LBM-based numerical methodology for solving the transient RTE and bio-heat transfer model has now been employed for investigating the influence of an optical inhomogeneity embedded within the body of the tissue phantom on the resultant temperature distribution. The inhomogeneities considered are absorbing as well as scattering in nature. The ratio of the absorption/scattering
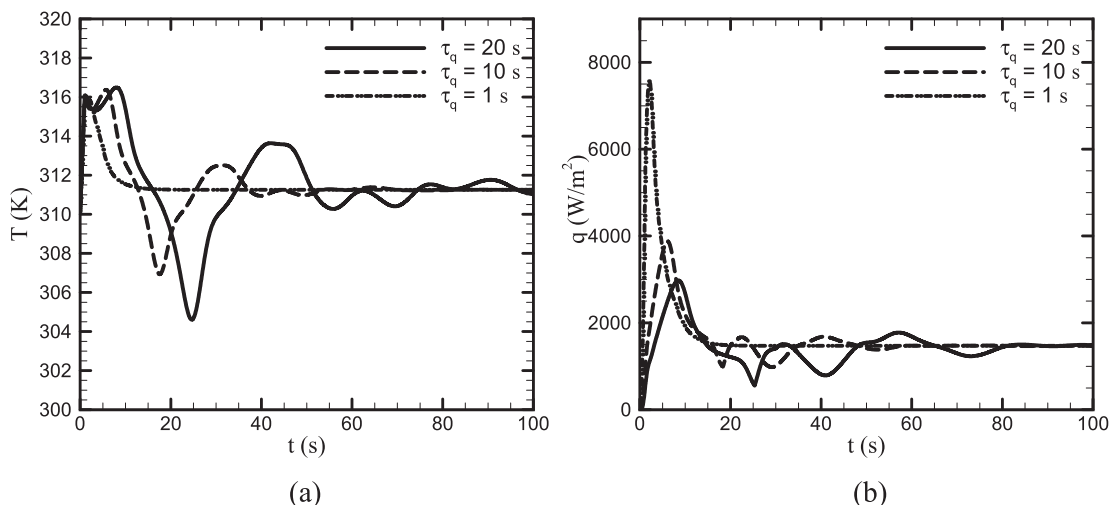

Fig. 8. Temporal distribution of (a) temperature, (b) heat flux at center (Location 1) for $\tau_T = 0.1$ s.

coefficients of the embedded inhomogeneities with respect to those of the homogenous tissue phantom medium i.e. the contrast level has been set to be equal to 2:1. The optical properties of the uniform homogeneous medium have already mentioned in Section 3. The absorption inhomogeneity numerically simulates the existence of malignant cells, while the abnormal cells that are benign in nature have been simulated in the form of scattering inhomogeneity.

4.3.1. Absorption inhomogeneity

The assessment of the influence of an inhomogeneity that is purely absorbing in nature and has a contrast level of 2:1 on the temperature distribution within the tissue phantom subjected to laser irradiation has been presented in this section. The inhomogeneity dimensions are 0.4 mm × 0.4 mm and the co-ordinates of its south–west corner are $x = 0.8$ mm, $y = 0.8$ mm while the north–east corner is located at $x = 1.2$ mm, $y = 1.2$ mm. The two-dimensional temperature field within the body of the tissue phantom that is embedded with an absorbing inhomogeneity has been shown in Fig. 10(b). For comparison, the corresponding thermal profiles for the homogeneous tissue phantom have also been presented in the figure (Fig. 10(a). As expected, the maximum temperature at any given time instant is realized at the point of laser irradiation. It is to be seen that in the case of absorbing inhomogeneity, the thermal energy is primarily localized within the spatial region covered by the dimensions of the embedded inhomogeneity. The localization of the thermal energy in this region leads to an increase in its temperature as compared to the surrounding domain. This localized increase in the temperature corresponding to the physical extent of the embedded inhomogeneity is expected because the absorption coefficient of the inhomogeneity is twice that of the homogeneous background medium. This in turn leads to the absorption of higher amount of thermal energy, which increases the temperature of this region locally. On the other hand, the temperature distribution is nearly

uniform without any localized increase in temperature at any spatial location in the case of homogeneous tissue phantom (Fig. 10(a)).

Fig. 11 shows the temporal variation of temperature based on DPL model at the center (Location 1) for the case of the tissue phantom that is embedded with an absorption inhomogeneity. For comparison, the corresponding profile for the homogeneous phantom has also been presented. One achieves the maximum temperature rise during the first 1 s time duration and it corresponds to the case of the absorbing nature of the embedded inhomogeneity (that replicate the rapidly growing malignant cells) that absorbs relatively larger part of the thermal energy in comparison with that absorbed by a purely homogeneous tissue
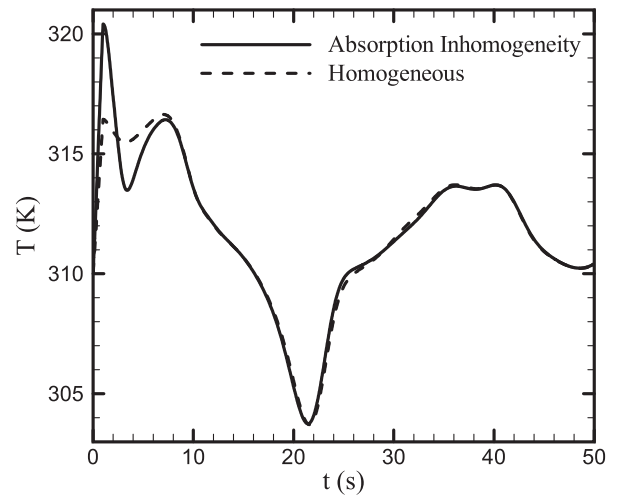

Fig. 11. Effect of absorption inhomogeneity on temporal profile of temperature at center (Location 1).

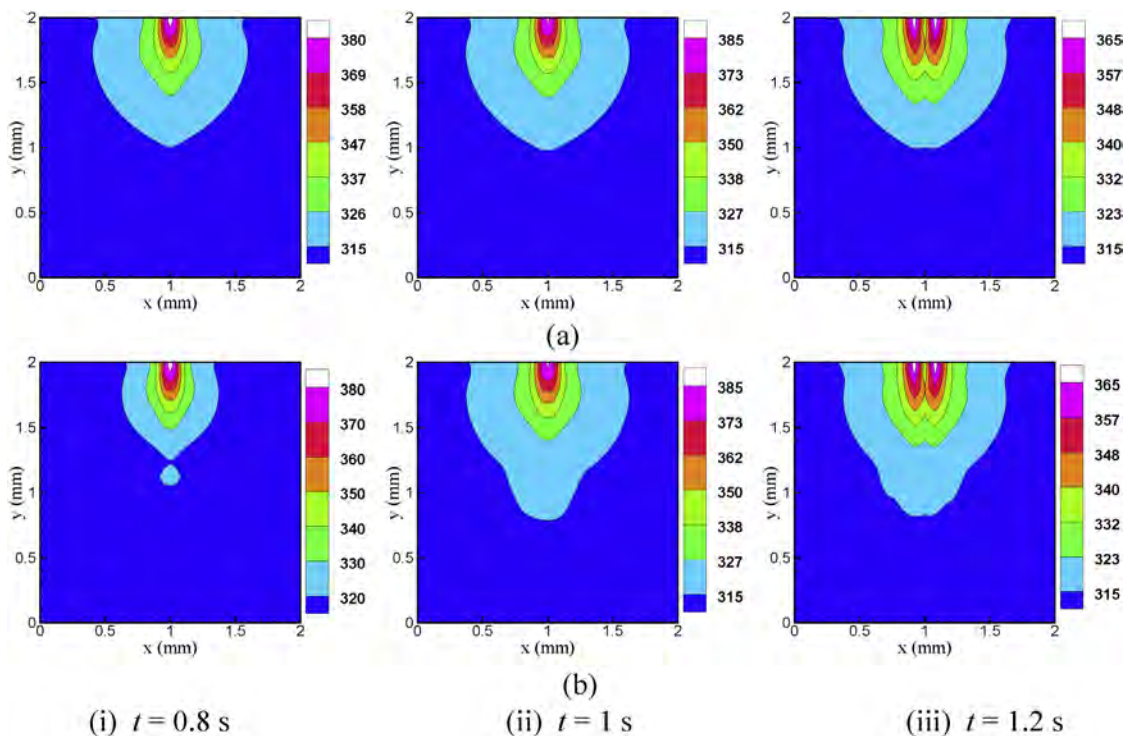(i) $t = 0.8$ s   (ii) $t = 1$ s   (iii) $t = 1.2$ s

Fig. 10. Temperature contours at various time instants for (a) homogeneous phantom and (b) tissue phantom embedded with absorption inhomogeneity.

phantom (or the background medium), thereby leading to a sharp increase in the local temperature values. Another interesting observation that can be made from the temperature profiles shown in Fig. 11 can be made in the form of extent/ magnitude of oscillations during the period of laser irradiation. Comparatively stronger oscillations in the temporal profiles of temperature are to be seen in the case of tissue phantom that is embedded with absorbing inhomogeneity during the initial time period i.e. $t < 5$ s than those observed for the homogeneous tissue phantom. Once the laser power is switched off, irrespective of the case considered, the thermal energy absorbed within the localized region corresponding to the spatial extent of the inhomogeneity starts getting diffused into its surrounding and since a finite value of relaxation time is associated with the heat flux ($\tau_q = 15$ s), the heat diffusion phenomenon is accompanied with oscillations due to the wave nature of propagating thermal front as predicted by DPL-based model. As expected, at higher time instants, the temperature profiles for both the cases overlap with each other.

A detailed comparison of two-dimensional temperature distributions achieved in the case of a homogeneous and non-homogeneous (embedded with absorption inhomogeneity) tissue phantoms is presented in Fig. 12. Temperature distributions corresponding to three different time instants $t = 1$ s, $t = 2$ s and $t = 4$ s are shown. It is to be seen from Fig. 12(i) that the presence of absorbing inhomogeneity results into a localized increase in temperature within the region that is spread over the physical size of the embedded inhomogeneity. At any given time instant, the local temperature at the site of embedded inhomogeneity is considerably higher than that achieved at the same spatial location in the case of homogeneous tissue phantom. This is understandable as by virtue of the absorbing nature, the inhomogeneity (replicating the rapidly multiplying abnormal cells) absorbs relatively larger amount of thermal energy in comparison with the surrounding normal cells, thereby leading to a localized increase in temperature in the region over which it is spread.

An interesting observation can be made in terms of oscillations in the temperature distribution in the region
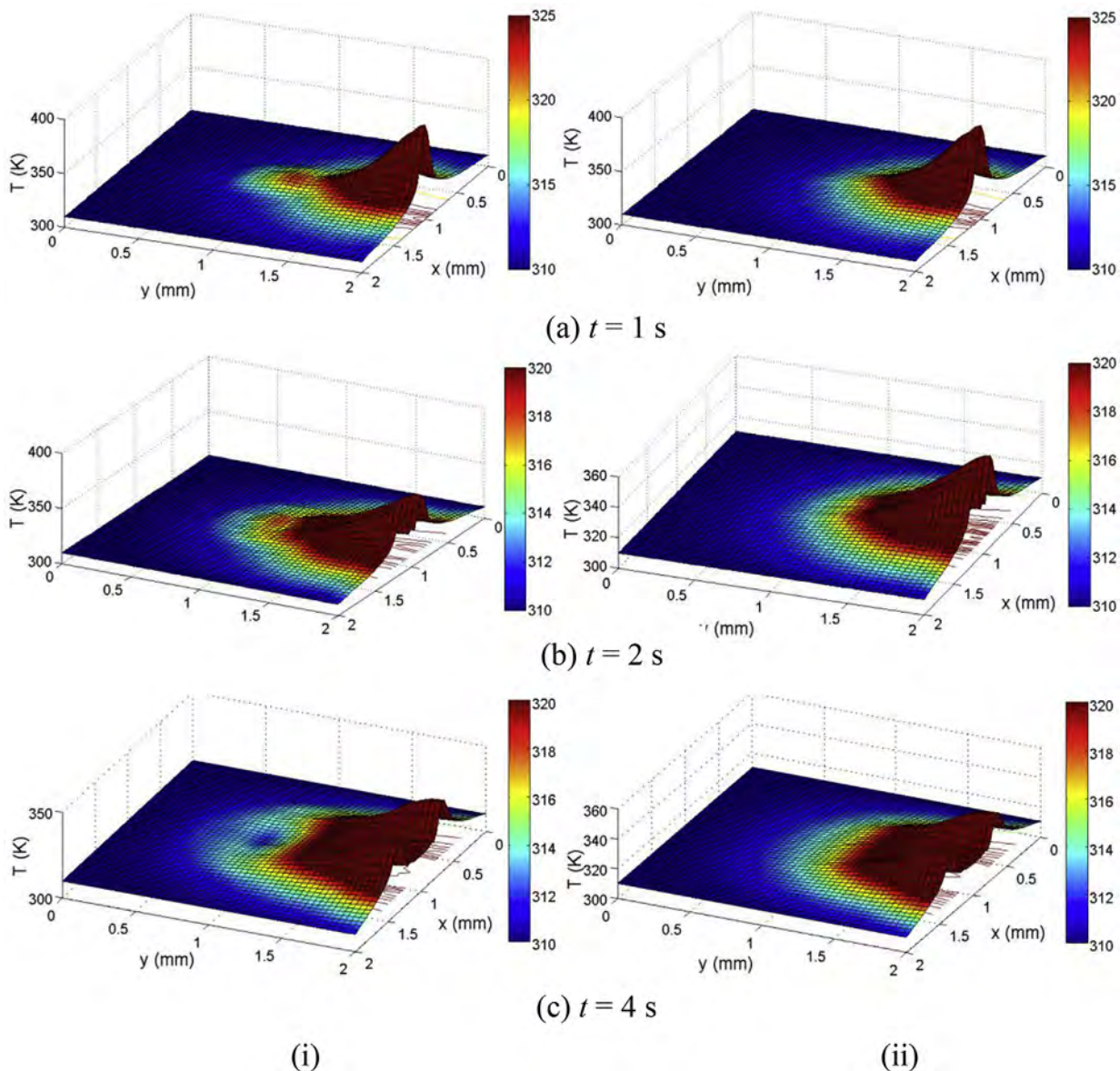

(a) $t = 1$ s

(b) $t = 2$ s

(c) $t = 4$ s

(i)   (ii)

Fig. 12. Two-dimensional temperature distributions at various time instants for (i) absorption inhomogeneity embedded phantom and (ii) homogenous phantom.

surrounding the absorption inhomogeneity on the basis of surface plots shown for time instants greater than $t = 1$ s. Relatively strong oscillations in the thermal profiles (2-D temperature distribution) are to be seen in the spatial region around the embedded inhomogeneity as can be seen from Fig. 12(b) and (c). These observation, as made through Fig. 12(i), become important in the context of photo-thermal therapy wherein the prime interest is in achieving localized increase in the temperature at the affected region without raising the temperature of the surrounding healthy tissues. The results of the analysis, as predicted through Fig. 12, provide a basis of determining the extent of thermal energy penetration in the region surrounding the embedded inhomogeneity and hence accordingly, the operating parameters (e.g. laser power, irradiation time etc.) can be controlled so as to impart minimum damage to the surrounding homogeneous medium.

4.3.2. Scattering inhomogeneity

This section discusses the influence of an inhomogeneity that is purely scattering in nature on the temperature distributions achieved as the tissue phantom is subjected to laser irradiation. The dimensions and the position of the inhomogeneity considered in this case are the same as that mentioned for the absorption inhomogeneity in the previous section. The absorption coefficient for the inhomogeneity equals to that of the homogeneous background and is kept constant. The scattering properties of the inhomogeneity have been considered such that the resultant contrast level is 2:1. Fig. 13 shows the temporal variation of temperature predicted by the DPL-based model at the center of the tissue phantom (Location 1) that is embedded with a scattering inhomogeneity. It is to be seen that the impact of the presence of scattering inhomogeneity on thermal profiles inside the tissue phantom is quite negligible and is in contrast with the observation that was made in the previous section that pertained to the presence of a purely absorbing inhomogeneity. The observed trend of the profiles shown in Fig. 13 can be explained by the fact that an increase in scattering coefficient of the medium leads to increased number of scattering events and thus the smaller amount of energy gets stored as compared to the case of absorption inhomogeneity while due to scattering temperature rise is more than that is observed in homogeneous medium.
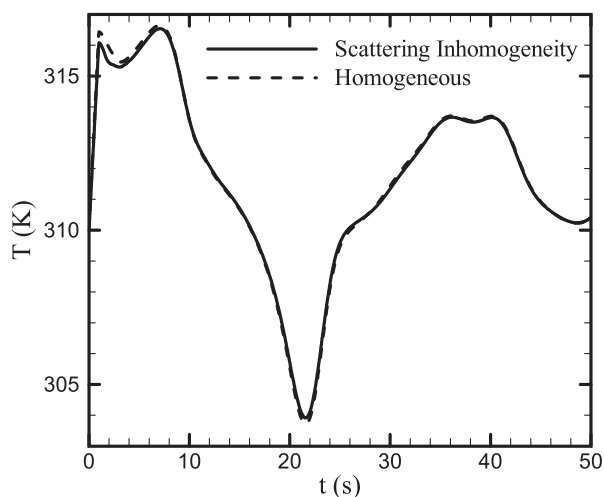

Fig. 13. Effect of scattering inhomogeneity on temporal profile of temperature at center (Location 1).

5. Conclusions

Lattice Boltzmann method (LBM)-based numerical scheme has been developed and employed for solving the coupled transient RTE and dual-phase lag (DPL) heat conduction model to understand the thermal response of laser-irradiated biological tissue phantoms. The tissue phantom has been subjected to short pulse laser irradiation and the intensity distribution inside the tissue phantom medium has been estimated by solving the transient form of RTE. The solution of the time-dependent RTE has been coupled with a generalized non-Fourier heat conduction model i.e. DPL. The numerical scheme has been verified against the results available in the literature. Results of study reveal that the uniform solver that is based on the concept of LBM successfully predicts the thermal response of the laser-irradiated biological tissue phantoms, both in terms of intensity distribution as well as the resultant temperature profiles. The inherent wave nature of the thermal propagation front traveling through the body of the tissue phantom has successfully been captured by the DPL-based heat conduction model. The initial transients of the thermal field evolution showed the oscillatory behavior of temperature field at any given spatial location, while a nearly uniform diffusion of thermal energy was predicted at higher time instants. The oscillations in the temperature field were found to be strongly affected by the thermal relaxation times associated with the temperature gradient (τ_T) and heat flux (τ_q). The presence of abnormal cells (malignant and/or benign) embedded in an otherwise homogeneous medium have been simulated in the form of absorption and scattering inhomogeneities within the body of the biological tissue phantom. It is demonstrated that the absorption inhomogeneities lead to localized increase in temperature, the extent of which is spread over the spatial dimension of the embedded inhomogeneity. On the other hand, one does not observe any significant changes in the temperature distribution in the case of scattering inhomogeneity. The present work is important in the context of photo-thermal therapy as it employs for the first time, to the best of the knowledge of the authors, the LBM-based numerical scheme for handling the coupled transient RTE and non-Fourier heat conduction model for determining the temperature distribution within the body of the laser-irradiated tissue-mimicking biological phantoms.

References

[1] R.W.Y. Habash, R. Bansal, D. Krewski, H.T. Alhafid, Thermal therapy, part III: ablation techniques, Crit. Rev. Biomed. Eng. 35 (1–2) (2007) 37–121.

[2] P.K. Gupta, N. Ghosh, H.S. Patel, Lasers and laser tissue interaction, in: A. Kishen, A. Asundi (Eds.), Fundamentals and Applications of Biophotonics in Dentistry, Imperial College Press, London, 2007, pp. 123–148.

[3] L.A. Dombrovsky, V. Timchenko, M. Jackson, Indirect heating strategy of laser induced hyperthermia: an advanced thermal model, Int. J. Heat Mass Transfer 55 (2012) 4688–4700.

[4] L.A. Dombrovsky, J.H. Randrianalisoa, W. Lipinski, V. Timchenko, Simplified approaches to radiative transfer simulations in laser induced hyperthermia of superficial tumors, Comput. Therm. Sci. 5 (2013) 521–530.

[5] J.H. Randrianalisoa, L.A. Dombrovsky, W. Lipinski, V. Timchenko, Effects of short-pulsed laser radiation on transient heating of superficial human tissues, Int. J. Heat Mass Transfer 78 (2014) 488–497.

[6] N.G. Khlebtzov, L.A. Dykman, Optical properties and biomedical applications of plasmonic nanoparticles, J. Quant. Spectrosc. Radiat. Transfer 111 (2010) 1–35.

[7] Y. Bayazitoglu, S. Kheradmand, T.K. Tullius, An overview of nanoparticle assisted laser therapy, Int. J. Heat Mass Transfer 67 (2013) 469–486.

[8] S. Chandrasekhar, Radiative Transfer, Dover Publications Inc., New York, 1960, p. 393.

[9] S. Kumar, A. Srivastava, Thermal analysis of laser-irradiated tissue phantoms using dual phase lag model coupled with transient radiative transfer equation, Int. J. Heat Mass Transfer 90 (2015) 466–479.

[10] A.J. Welch, M.J.C.V. Gemert, W.M. Star, Definitions and overview of tissue optics, in: A.J. Welch, M.J.C.V. Gemert (Eds.), Optical-thermal Response of Laser-irradiated Tissue, Springer, New York, 2011, pp. 27–66.

[11] S. Kumar, A. Srivastava, Numerical investigation of thermal response of laser irradiated tissue phantoms embedded with optical inhomgeneities, Int. J. Heat Mass Transfer 77 (2014) 262—277.
[12] H. Schweiger, A. Oliva, M. Costa, C.D.P. Segarra, A Monte Carlo method for the simulation of transient radiation heat transfer: application to compound honeycomb transparent insulation, Numer. Heat Transfer B 35 (2001) 113—136.
[13] Z. Guo, J. Aber, B. Garetz, S. Kumar, Monte Carlo simulation and experiments of pulsed radiative transfer, J. Quant. Spectrosc. Radiat. Transfer 73 (2002) 159—168.
[14] Z. Guo, S. Kumar, Discrete-ordinates solution of short-pulsed laser transport in two-dimensional turbid media, Appl. Opt. 40 (2001) 3156—3163.
[15] M. Sakami, K. Mitra, P.F. Hsu, Analysis of light-pulse transport through two-dimensional scattering and absorbing media, J. Quant. Spectrosc. Radiat. Transfer 73 (2002) 169—179.
[16] S.C. Mishra, P. Chugh, P. Kumar, K. Mitra, Development and comparison of the DTM, the DOM and the FVM formulations for the short pulse laser transport through a participating medium, Int. J. Heat Mass Transfer 49 (11—12) (2006) 1820—1832.
[17] C. Das, A. Trivedi, K. Mitra, T. Vo-Dinh, Short pulse laser propagation through tissues for biomedical imaging, J. Phys. D. Appl. Phys. 36 (2003) 1—8.
[18] P. Asinari, S.C. Mishra, R. Borchiellini, A lattice Boltzmann formulation to the analysis of radiative heat transfer problems in a participating medium, Numer. Heat Transfer B 57 (2010) 126—146.
[19] S.C. Mishra, R.R. Vernekar, Analysis of transport of collimated radiation in a participating media using the lattice Boltzmann method, J. Quant. Spectrosc. Radiat. Transfer 113 (2012) 2088—2099.
[20] R.R. Vernekar, S.C. Mishra, Analysis of transport of short-pulse radiation in a participating medium using lattice Boltzmann method, Int. J. Heat Mass Transfer 77 (2014) 218—229.
[21] X. He, S. Chen, R. Zhang, Lattice Boltzmann scheme for incompressible multiphase flow and its application in simulation of Rayleigh—Taylor instability, J. Comput. Phys. 152 (1999) 642—663.
[22] S. Succi, The Lattice Boltzmann Method for Fluid Dynamics and Beyond, Oxford University Press, London, 2001.
[23] W.S. Jiaung, J.R. Ho, C.P. Kuo, Lattice Boltzmann method for heat conduction problem with phase change, Numer. Heat Transfer B 39 (2001) 167—187.
[24] D. Wolf-Gladrow, Lattice-gas Cellular Automata and Lattice Boltzmann Models: an Introduction, Springer-Verlag, Berlin, Heidelberg, 2000.
[25] H.H. Pennes, Analysis of tissue and arterial blood temperatures in the resting forearm, J. Appl. Physiol. 1 (1948) 93—122.
[26] C. Cattaneo, A form of heat conduction equation which eliminates the paradox of instantaneous propagation, Comptes Rendus 247 (1958) 431—433.
[27] P. Vernotte, Some possible complications in the phenomena of thermal conduction, Comptes Rendus 252 (1961) 2190—2191.
[28] C. Korner, H.W. Bergmann, The physical defects of the hyperbolic heat conduction equation, Appl. Phys. A 67 (1998) 397—401.
[29] C. Bai, A.S. Lavine, On the hyperbolic heat conduction and the second law of thermodynamics, J. Heat Transfer ASME Trans. 117 (1995) 256—263.
[30] T.J. Bright, Z.M. Zhang, Common misperceptions of the hyperbolic heat equation, AIAA J. Thermophys. Heat Transfer 23 (2009) 601—607.
[31] Z.M. Zhang, T.J. Bright, G.P. Peterson, Reexamination of the statistical derivations of Fourier's law and Cattaneo's equation, Nanoscale Microscale Thermophys. Eng. 15 (2011) 220—228.
[32] D.T. Tzou, A unified field approach for heat conduction from macro to microscales, ASME J. Heat Transfer 117 (1995) 8—16.
[33] N. Afrin, J. Zhou, Y. Zhang, D.Y. Tzou, J.K. Chen, Numerical simulation of thermal damage to living biological tissues induced by laser irradiation based on a generalized dual phase lag model, Numer. Heat Transfer A 61 (2012) 483—501.
[34] D.Y. Tzou, J.K. Chen, Thermal lagging in random media, J. Thermophys. Heat Transfer 12 (1998) 567—574.
[35] S.A. Rukolaine, Unphysical effects of the dual-phase-lag model of heat conduction, Int. J. Heat Mass Transfer 78 (2014) 58—63.
[36] Y. Sun, X. Zhang, Analysis of transient conduction and radiation problems using the lattice Boltzmann and discrete ordinates methods, Numer. Heat Transfer A 68 (2015) 619—637.
[37] R. Raj, A. Prasad, P.R. Parida, S.C. Mishra, Analysis of solidification of a semi-transparent planar layer using the lattice Boltzmann method and the discrete transfer method, Numer. Heat Transfer A 49 (2006) 279—299.
[38] B. Mondal, S.C. Mishra, Lattice Boltzmann method applied to the solution of the energy equations of the transient conduction and radiation problems on non-uniform lattices, Int. J. Heat Mass Transfer 51 (2008) 68—82.
[39] S.C. Mishra, H. Poonia, R. Vernekar, A.K. Das, Lattice Boltzmann method applied to the analysis of radiative transport problems with and without conduction in a 1-D planar medium, Heat Transfer Eng. 35 (2014) 1267—1278.
[40] S.C. Mishra, H. Poonia, A.K. Das, P. Asinari, R. Borchiellini, Analysis of conduction—radiation heat transfer in 2-D enclosure using the lattice Boltzmann method, Numer. Heat Transfer A 66 (2014) 669—688.
[41] A.N. Bashkatov, E.A. Genina, V.V. Tuchin, Optical properties of skin, subcutaneous and muscle tissues: a review, J. Innov. Opt. Health Sci. 4 (2011) 9—38.
[42] S.L. Jacques, Optical properties of biological tissues: a review, Phys. Med. Biol. 58 (2013) R37—R61.
[43] D.Y. Tzou, in: Macro-to Microscale Heat Transfer: the Lagging Behavior, Taylor and Francis, Washington, DC, 1996, pp. 25—29.
[44] P.J. Antaki, New interpretation of non-Fourier heat conduction in processed meat, ASME J. Heat Transfer 127 (2005) 189—193.
[45] M. Salloum, N. Ghaddar, K. Ghali, A new transient bioheat model of the human body and its integration to clothing models, Int. J. Therm. Sci. 46 (2007) 371—384.
[46] J. Jiao, Z. Guo, Thermal interaction of short-pulsed laser focused beams with skin tissues, Phys. Med. Biol. 54 (2009) 4225—4241.
[47] M. Jaunich, S. Raje, K. Kim, K. Mitra, Z. Guo, Bio-heat transfer analysis during short pulse laser irradiation of tissues, Int. J. Heat Mass Transfer 51 (2008) 5511—5521.
[48] K. Kim, Z. Guo, Multi-time-scale heat transfer modeling of turbid tissues exposed to short-pulsed irradiations, Comput. Methods Prog. Biomed. 86 (2007) 112—123.
[49] J.L. Boulnois, Photophysical processes in recent medical laser developments: a review, Lasers Med. Sci. 1 (1986) 47—66.
[50] A. Katzir, Lasers and Optical Fibers in Medicine, Academic Press, California, 1993.
[51] X. He, L.S. Luo, A priori derivation of the lattice Boltzmann equation, Phys. Rev. E 55 (1997) 6811—6817.
[52] J.R. Ho, C.P. Kuo, W.S. Jiaung, Study of heat transfer in multilayered structure within the framework of dual-phase-lag heat conduction model using lattice Boltzmann method, Int. J. Heat Mass Transfer 46 (2003) 55—69.
[53] A. Gunstensen, Lattice Boltzmann model of immiscible fluids, Phys. Rev. A 43 (1991) 4320—4327.
[54] S. Chen, G.D. Doolen, Lattice Boltzmann method for fluid flows, Annu. Rev. Fluid Mech. 30 (1998) 329—364.
[55] C.Y. Yang, Direct and inverse solutions of the two-dimensional hyperbolic heat conduction problems, Appl. Math. Model. 33 (2009) 2907—2918.
[56] B. Shen, P. Zhang, Notable physical anomalies manifested in non-Fourier heat conduction under the dual-phase-lag model, Int. J. Heat Mass Transfer 51 (2008) 1713—1727.
[57] K. Mitra, S. Kumar, A. Vedavaraz, M. Moallemi, Experimental evidence of hyperbolic heat conduction in processed meat, J. Heat Transfer 117 (1995) 568—573.